Polarization phase-shifting point-diffraction interferometer

Robert M. Neal and James C. Wyant

A new instrument, the polarization phase-shifting point-diffraction interferometer, has been developed by use of a birefringent pinhole plate. The interferometer uses polarization to separate the test and reference beams, interfering what begin as orthogonal polarization states. The instrument is compact, simple to align, and vibration insensitive and can phase shift without moving parts or separate reference optics. The theory of the interferometer is presented, along with properties and fabrication techniques for the birefringent pinhole plate and a new model used to determine the quality of the reference wavefront from the pinhole as a function of pinhole size and test optic aberrations. The performance of the interferometer is also presented, along with a detailed error analysis and experimental results. © 2006 Optical Society of America

OCIS codes: 120.3180, 120.3940, 120.5050, 120.6650.

1. Introduction

As technology increases, so does the need for faster, more accurate metrology equipment. With the need for higher accuracy, the physical limitations of current interferometers are becoming restrictive. Overcoming these limitations by using current techniques means building more-complicated systems or increasing computation time. New interferometer designs make it possible to increase the speed and accuracy of interferometric measurements while maintaining a relatively simple system.

To date, despite their obvious advantages for optical testing, common-path interferometers, such as scatterplate, Fresnel zone plate, and point-diffraction interferometers, have been largely neglected for use in phase-shifting interferometry, primarily because of the difficulty of phase shifting a common-path interferometer. The common-path design provides significantly increased environmental stability and decreased system complexity. Unfortunately, the common-path design also causes problems in separating the test and reference beams. With both beams traversing the same path, adding phase in one beam without adding it to the other becomes difficult, thus making phase-shifting difficult.

A few groups of scientists have found clever ways of phase shifting the point-diffraction interferometer (PDI). The first to phase shift the PDI was Kwon, who fabricated a pinhole in a sinusoidal transmission grating to produce three simultaneous phase-shifted interferograms.[1] Kadono *et al.* were next to phase shift the PDI by utilizing a series of polarization optics with a pinhole constructed in one of the linear polarizers.[2] Kadono *et al.* later developed a second phase-shifting PDI by etching a small pinhole in the electrodes of a liquid-crystal variable retarder.[3] Without the electrodes, the liquid crystals inside the pinhole do not change phase with applied voltage. Later, Mercer and Creath phase shifted a similar PDI by embedding a glass microsphere in a thin liquid-crystal retarder.[4] The microsphere created the reference wavefront, and the liquid crystal produced the variable phase shift. Most recently, Totzeck *et al.* created a phase-shifting PDI by fabricating a small pinhole in a mica half-wave plate, followed by a variable retarder.[5] Immediately after the pinhole, the test and reference beams have orthogonal polarizations, which are phase shifted after the beams pass through the variable retarder. In each of these cases, the phase shifting is done at, or near, the pinhole, leading to complex pinhole assemblies and the chance for increased errors.

The polarization phase-shifting point-diffraction interferometer (PPSPDI) presented in this paper also uses polarization to separate the test and reference beams through the use of a birefringent pinhole plate, interfering what begin as orthogonal polarization

When this research was performed, the authors were with the Optical Sciences Center, University of Arizona, Tucson, Arizona 85721. R. M. Neal is now with ITT Industries, Inc., AES Division, 5901 Indian School Road NE, Albuquerque, New Mexico 87110. R. Neal's e-mail address is mark.neal@itt.com. J. C. Wyant's e-mail address is jcwyant@optics.arizona.edu.

Received 13 July 2005; revised 14 December 2005; accepted 24 December 2005; posted 4 January 2006 (Doc. ID 63406).
0003-6935/06/153463-14$15.00/0

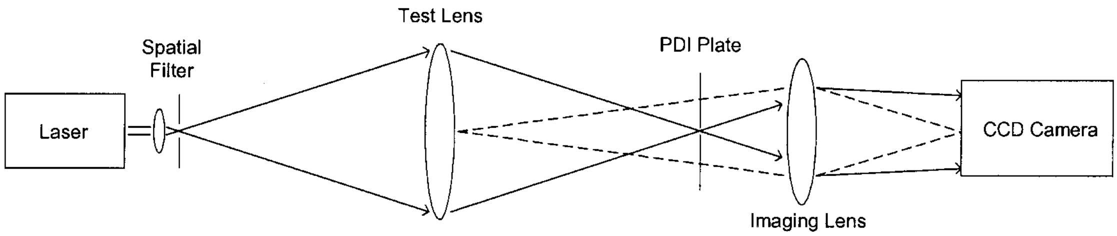

Fig. 1. Conventional PDI.

states. One then accomplishes phase shifting by simply varying the polarization state of the laser source. This method greatly simplifies construction of the pinhole plate and reduces the possible sources of error.

2. Conventional Point-Diffraction Interferometer

The conventional PDI is a simple common-path interferometer capable of directly measuring optical wavefronts for metrology and optical testing. The PDI's primary advantage is its common-path design, in which the test and reference beams travel the same or almost the same path. This design makes the PDI extremely useful when environmental isolation is not possible or a reduction in the number of precision optics is required.

The PDI is a simple two-beam interferometer whose reference beam is created from a portion of the test beam by diffraction by means of a small pinhole in a semitransparent coating. The operation of the PDI is shown in Fig. 1.

Light from the laser is sent into a spatial filter whose pinhole acts as a point source for the test lens. The spatial filter is positioned at twice the focal distance in front of the test lens to simulate a 4-*f* imaging system with a magnification of -1. The spatial filter pinhole is chosen sufficiently small that the size of the focus spot formed by the test lens is due solely to the diffraction limit of the test lens plus aberrations. The PDI plate, which one creates by placing a small pinhole in a semitransparent coating, is placed at the focus spot of the test lens. The experimental setup can be modified such that collimated light is incident onto the test lens, producing a focus spot at the back focal distance of the test lens. The diameter of the pinhole created is approximately half of the unaberrated Airy disk diameter of the test lens,[6] or

$$d_{\text{pinhole}} \approx 1.22\lambda\ (f\#_{\text{working}}). \tag{1}$$

This requirement sets the lower limit on the *f*-number of a particular optic that can be tested for a given pinhole diameter. A 5 μm diameter pinhole can be used to test optics with working *f*-numbers of 6.5 and larger. The pinhole is aligned such that it is coincident with a portion, usually the center, of the focus spot formed by the test lens. The portion of light incident upon the pinhole is diffracted by the aperture into a spherical wavefront that serves as the reference wavefront for the interferometer. The diameter constraint of the pinhole produces a reference wavefront with only minimal amplitude and phase variations.[6] The remainder of the light from the test lens is attenuated but is otherwise transmitted unaffected through the semitransparent region surrounding the pinhole, as shown in Fig. 2. With the PDI pinhole smaller than the Airy disk radius of the test lens, the angular subtense of the diffracted reference beam will always be larger than the angular subtense of the test beam, thus ensuring that the entire optic is tested.

The test and reference wavefronts pass through the imaging optics, which form an image of the test lens that is superimposed with interference fringes on the CCD camera. For good fringe contrast, the test beam is carefully attenuated such that the relative intensities of the test and reference beams are similar. Typical transmittances of the PDI plate are 0.01 to 0.1.[7]

3. Polarization Phase-Shifting Point-Diffraction Interferometer

The PPSPDI is a modification of the conventional PDI that uses polarization changes in the incident beam to induce a phase shift. The PPSPDI retains the common-path design and advantages of the conventional PDI, while the novel PDI filter allows for phase shifting and increased accuracy in phase measurement. The difference in the design lies in the construction of the PDI filter. In the conventional PDI, the filter is a partially transmitting pinhole plate, but the PDI filter in the PPSPDI is a pinhole etched into a thin-film half-wave plate.

The PPSPDI laboratory experiment is illustrated in Fig. 3. Light from the laser operating at 632.8 nm passes through the combination of a polarizer and a

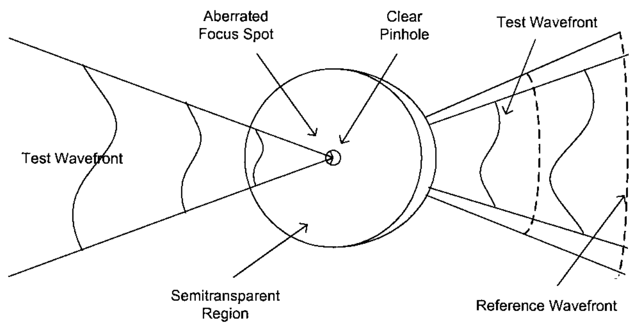

Fig. 2. Operation of the PDI Plate.

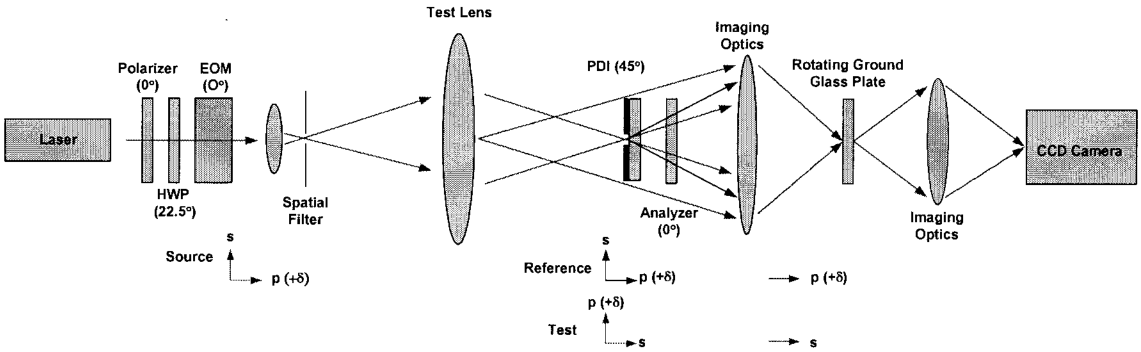

Fig. 3. Operation of the PPSPDI.

half-wave plate (HWP). The polarizer, oriented at 0°, is used to isolate a single, linear polarization state, while the half-wave plate at 22.5° rotates the polarization state such that its output is linearly polarized at 45°. The polarizer–half-wave-plate combination ensures selection of linear polarization at any desired angle by rotation of the half-wave plate. Following this combination is an electro-optic modulator (EOM) with electrodes oriented vertically (0°), that is, used as the phase shifter for the interferometer. When a voltage is applied to the modulator, the index ellipsoid of the crystal inside the modulator rotates, producing a change in the index of refraction of the crystal in the plane perpendicular to the electrodes. In propagating through the crystal, the two orthogonal states, horizontal and vertical, will encounter a constant natural phase difference without an applied field owing to the nature of the crystal and an electrically induced phase difference that increases linearly with the applied field. Because of this, the horizontal component, p, encounters a larger optical path through the crystal and is given an extra phase, δ, that one changes by varying the field applied to the modulator. Recombining the orthogonal components, in general, produces elliptical polarization in the output of the modulator. Following the modulator is a spatial filter with a 5 μm pinhole. The spatial filter acts as a point source and is positioned at twice the focal distance in front of the test lens to simulate a 4-f imaging system with a magnification of -1. The spatial filter pinhole is small, so the size of the focus spot formed by the test lens is due solely to the diffraction limit of the lens plus aberrations. The test lens forms an aberrated focus spot on the PDI plate, located at twice the focal distance behind the test lens. One constructs the pinhole plate by etching the pinhole through a birefringent silicon thin-film half-wave plate with the fast axis oriented at 45° to the orthogonal components of the incident beam, s and p. As with the conventional PDI, the diameter of the pinhole created is approximately half the unaberrated Airy disk diameter of the test lens,[6] or

$$d_{\text{pinhole}} \approx 1.22\lambda\ (f\#_{\text{working}}), \tag{2}$$

where the working f-number of the test lens in a 4-f imaging system is twice the actual lens f-number. Again, the clear pinhole is aligned such that it is coincident with the center of the focus spot formed by the test lens. The portion of light incident on the pinhole does not encounter the thin-film half-wave plate and is diffracted into a spherical reference wavefront, retaining the elliptical polarization state of the incident beam. The thin film half-wave plate transmits and attenuates the remainder of the light from the test lens and rotates the s and p orthogonal states by 90°; the s and p states emerge orthogonal but flipped in orientation, as shown in Fig. 4. This wavefront retains the aberrations of the incident wavefront and serves as the test wavefront for the interferometer.

An analyzer with its transmission axis horizontal placed after the PDI plate isolates one set of orthogonal components from the test and reference beams. Moreover, the analyzer produces two interfering wavefronts, the test and reference wavefronts, with a variable phase difference between them. By varying the voltage applied to the electro-optic modulator, one can vary the phase difference between the test and reference wavefronts, causing phase shifting. Both wavefronts then pass through imaging optics, which image the plane of test lens onto a rotating ground glass plate. Interference fringes are superimposed upon the image of the test lens on the rotating plate. The rotating ground glass plate reduces the coherence of the system, thereby reducing the spurious fringes from the protective glass plate in front of the CCD chip in the camera. The camera optics then

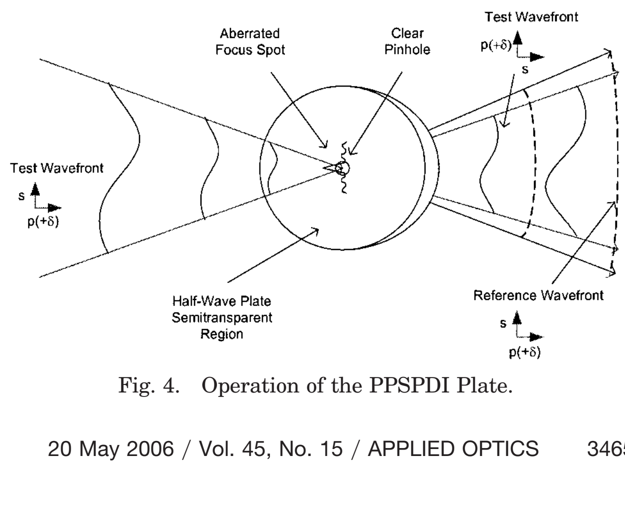

Fig. 4. Operation of the PPSPDI Plate.

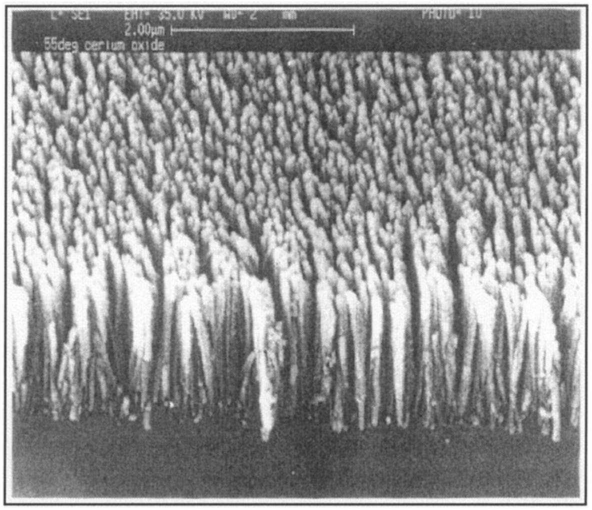

Fig. 5. Characteristic normal columnar structure for bidirectionally deposited birefringent films.[8]

image the interference pattern produced on the ground glass plate onto the CCD, as shown in Fig. 3.

4. Properties of the Birefringent Thin-Film and Manufacture of Pinholes

The most important component in the PPSPDI is a novel pinhole filter that we constructed by etching a pinhole into a half-wave-plate birefringent thin film. The film is deposited through a bidirectional deposition process presented below. Several methods to etch the pinhole into the film, such as reactive ion-beam etching and argon-ion milling, were attempted, but focused ion-beam etching, also discussed below, was found to be the best method for etching pinholes into the birefringent thin films. To our knowledge, we are the first to attempt to etch patterned features into such birefringent thin films.

A. Deposition and Properties of Birefringent Thin Films

The pinhole filter in the PPSPDI is created from a birefringent silicon thin film with a biaxial index structure. The locations of the three orthogonal principal dielectric axes and associated indices of refraction are fixed by the deposition geometry and symmetry.

Birefringent thin films are deposited in much the same way as isotropic films. In isotropic films, the evaporant material is heated in vacuum with either an electron beam gun or a heated coil, and the evaporant atoms travel from the source to the substrate, where they condense. The substrate, oriented at an angle θ to the evaporation source, is stationary, and the film grows with a tilted columnar microstructure. Limited mobility of the evaporant atoms along with self-shadowing causes the columnar structure growth. The condensing atoms are unable to move far enough to fill vacant positions in the shadow of existing material.[8]

In the case of the birefringent films, the substrate is not stationary during deposition. Evaporant atoms condense on the substrate, but after every few nanometers of deposition the substrate is rotated by 180°. Rotating the substrate causes the columnar microstructure to grow normally to the substrate, as illustrated in Fig. 5.

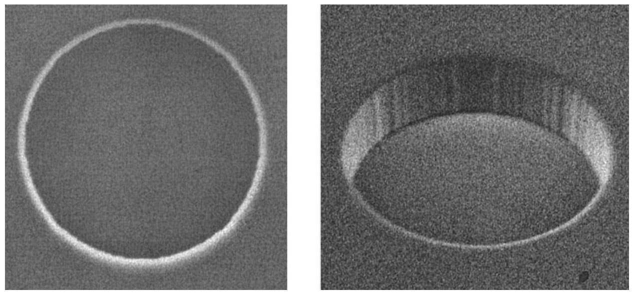

Fig. 6. Focused ion-beam-etched pinhole in a silicon thin film.

The material used for the films is silicon, which is not birefringent in typical oblique deposition. The birefringence in the thin films is caused by the normal columnar microstructure. This birefringence, which is due to the structure of the film as opposed to that of the material itself, is termed form birefringence. For form birefringence the columns are much thicker or are bunched preferentially in the direction perpendicular to the deposition plane, and typically both effects are present. This form birefringence depends on both the column shape and the packing density of the columns to cause direction-related variations in the refractive index. This deposition geometry, which causes the columnar structure to grow normally to the substrate, sets the orientations of the three principal dielectric axes: normal to the substrate (perpendicular to the columnar structure), perpendicular to the deposition plane, and parallel to the deposition plane.[8] The direction perpendicular to the deposition plane, which has a greater packing density of columns, has a large index of refraction, n_e, and is considered the slow axis for the retarder. The direction parallel to the deposition plane has a lower index of refraction, n_o, and is the fast axis for the retarder. The relationship that describes the retardance of the film in waves for a given wavelength λ is

$$R = (n_e - n_o)\,\frac{t}{\lambda} = \Delta n\,\frac{t}{\lambda}, \tag{3}$$

where the thickness of the film, t, determines the retardance. For a half-wave plate this gives a film thickness of

$$t = \frac{\lambda}{2\Delta n}. \tag{4}$$

The index difference, Δn, is not constant with wavelength and is given by a dispersion equation unique for each film material. Δn is a function of wavelength and for the silicon films is

$$\Delta n_\lambda = \Delta n_{633}\left[1 + c\left(\frac{1}{\lambda^2} - \frac{1}{633^2}\right)\right], \tag{5}$$

where c was experimentally determined as -268332 and Δn_{633} is 0.2816.[9]

Consequently, one may determine the index difference between the fast and slow axes for any wavelength and thus the total retardance at any wavelength for any known film thickness. Now, one may achieve the desired retardance by depositing a film of a specific, required thickness.

Although it was designed to be a half-wave plate, the film used in the PPSPDI was measured on an Axometrics Muller matrix polarimeter and found to have a retardance of 160° ± 0.5° and a diattenuation of 20% ± 0.5%. This difference was due to some problems in the deposition process and to uncertainty in monitoring the retardance *in situ*.

B. Focused Ion-Beam Etching

Focused ion-beam etching (FIBE) was found to be the best method to etch the pinhole in the silicon thin film. A focused ion-beam etcher operates similarly to a scanning-electron microscope, as both instruments take charged particles from a source, focus them into a beam, and then scan across small areas of a sample. A focused ion-beam etcher differs from an electron microscope by using gallium ions, instead of electrons, to form its beam. As gallium ions are orders of magnitude more massive than electrons, a FIBE's ion beam mills the sample surface instead of imaging it.[10] This etching method provides a way for maskless and resistless pinhole etching.

The FIBE uses a sharp tungsten needle wetted with gallium. The tip of the needle is subjected to high voltage, causing the ejection of gallium ions and acceleration toward the sample. The gallium ions are focused by electromagnetic fields into a highly focused beam and steered to a specific spot on the sample.[11] The kinetic energy of the ions as they strike the sample causes the ejection of atoms from the sample through a sputtering process. A wide variety of shapes is possible by variation of the scan rate, pattern, and energy of the ion beam as well as the dwell time of the beam at any given spot.

The focused ion-beam etching of the silicon films was done by Integrated Reliability Corporation of San Diego, California. The desired etch pattern is programmed into the computer controlling the FIBE that positions and scans the ion source to etch the features while leaving the remainder of the film untouched. The FEI FIB 200 system used has a lateral ion-beam resolution of 12 nm, which for a 5 μm pinhole gives a maximum etch error of 0.25%. It is possible to etch the feature profile to within 3° of vertical. An integrated high-magnification microscope was used to image the etched pinhole pictured in Fig. 6.

Focused ion-beam etching produced the best result of all etch methods attempted and is the best choice for the process to create the pinholes for the PPSPDI. While it required the fewest steps to complete, it produced features with high lateral resolution and near-vertical edge profiles.

5. Sources of Error

A mathematical model has been developed to investigate systematic errors in the PPSPDI. Because the test and reference beams are separated by polarization state, the PPSPDI is exceptionally sensitive to errors in the alignments and retardances of its various polarization optics. The three most important of these are the retardance of the thin film used to construct the pinhole filter, the angle of the fast axis of the film, and the angle of the final analyzer used to obtain the interference between the test and reference wavefronts. In turn, these errors cause discrepancies in the phase shifts, intensity modulations between phase steps, and error in the final measured phase.

A. Generalized Jones Matrix Propagation

One can model the PPSPDI using Jones matrices. For completely polarized systems such as the PPSPDI, the system elements are represented by 2×2 matrices with the incident field represented by a 2×1 matrix. One accomplishes propagation of the beams by multiplying the incident field by the matrix for each element in the system, as follows:

$$\begin{bmatrix} E_x & \text{Output} \\ E_y & \text{Output} \end{bmatrix} = [\text{Final Element}]\ldots[\text{2nd Element}] \times [\text{1st Element}]\begin{bmatrix} E_x & \text{Input} \\ E_y & \text{Input} \end{bmatrix}. \tag{6}$$

For the Jones matrix model to be valid, the test and reference beams must propagate through the system separately. While this is a common-path interferometer, the test and reference beams encounter different optical effects at the pinhole plate, so they must be propagated separately. Both the test and the reference beams begin as a single linearly polarized beam at 45° passing through an electro-optic modulator that adds a temporal phase to the vertical orthogonal component. The mathematical equations are

$$A_{\text{Test}} = \frac{1}{\sqrt{2}}\begin{bmatrix} 1 & 0 \\ 0 & e^{i\delta} \end{bmatrix}\begin{pmatrix} 1 \\ 1 \end{pmatrix},$$

$$A_{\text{Ref}} = \frac{1}{\sqrt{2}}\begin{bmatrix} 1 & 0 \\ 0 & e^{i\delta} \end{bmatrix}\begin{pmatrix} A \\ A \end{pmatrix}, \tag{7}$$

where δ is the temporal phase shift introduced by the modulator and A is a beam balance constant determined by the properties of the pinhole filter, which we discuss presently. Next, the beams pass through the test optic, where a spatial phase, Δ, is added to both components. The spatial phase added to the test and reference beams is directly related to the optical path difference or surface error on the test optic. The test and reference beams are represented by

$$A_{\mathrm{Test}} = \frac{1}{\sqrt{2}} \begin{bmatrix} e^{i\Delta} & 0 \\ 0 & e^{i\Delta} \end{bmatrix} \begin{bmatrix} 1 & 0 \\ 0 & e^{i\delta} \end{bmatrix} \begin{pmatrix} 1 \\ 1 \end{pmatrix},$$

$$A_{\mathrm{Ref}} = \frac{1}{\sqrt{2}} \begin{bmatrix} e^{i\Delta} & 0 \\ 0 & e^{i\Delta} \end{bmatrix} \begin{bmatrix} 1 & 0 \\ 0 & e^{i\delta} \end{bmatrix} \begin{pmatrix} A \\ A \end{pmatrix}. \tag{8}$$

Other than in the beam balance factor, the two beams are identical up to this point. After the test optic, the beams are focused onto the PDI plate. The test beam passes through the thin-film retarder with retardance ϕ and a fast axis oriented at an angle θ from vertical, while the reference beam passes through the pinhole. The film used in the PPSPDI was measured on an Axometrics Muller matrix polarimeter and found to have a retardance of 160° ± 0.5° and diattenuation of 20% ± 0.5%. The diattenuation, which varied as a function of film thickness, was found to be a unique property of the silicon film. Different film materials will have different values of birefringence and diattenuation. As a result of the diattenuation, the film absorbs differently along the fast and slow axes. The diattenuation is due not to an error in the deposition of the film but instead to the large index difference, and therefore significantly different absorption coefficients, between the fast and slow axes of the film. The diattenuation in the thin film is 20%, meaning that the slow axis of the film transmits 80% of the light amplitude transmitted by the fast axis. The reference beam in passing through the pinhole loses the spatial phase associated with the test optic but retains the temporal phase from the electro-optic modulator. Accordingly, only the test beam is multiplied by the matrices associated with the rotated thin film, while the reference beam loses the matrix associated with the test optic. This is the point where the beam balance factor, A, becomes important. A is determined by the amount of light diffracted by the pinhole and absorption of the thin film, and it measures how much light is diffracted by the pinhole into the reference beam as opposed to transmitted by the film in the test beam. The closer the balance between the beams, the closer this value approaches unity. Experimentally, the transmission of the film along the fast axis is ~55%. For a moderately aberrated system, 25% of the incident light is assumed incident onto the pinhole, which is half the Airy disk size and centered in the focus spot of the test optic. For these values, A was assigned a value of 0.6: Therefore the Jones matrix representation of the beams after the pinhole plate is

$$A_{\mathrm{Test}} = \frac{1}{\sqrt{2}} \underbrace{\begin{bmatrix} \cos(-\theta) & \sin(-\theta) \\ -\sin(-\theta) & \cos(-\theta) \end{bmatrix}}_{\text{Rotation Matrix }(-\theta)} \underbrace{\begin{bmatrix} 0.8\, e^{i\phi} & 0 \\ 0 & 1 \end{bmatrix}}_{\substack{\text{Retarder of} \\ \text{Retardance } \phi \text{ and} \\ 0.8 \text{ Diattenuation}}} \underbrace{\begin{bmatrix} \cos(\theta) & \sin(\theta) \\ -\sin(\theta) & \cos(\theta) \end{bmatrix}}_{\text{Rotation Matrix }(\theta)} \begin{bmatrix} e^{i\Delta} & 0 \\ 0 & e^{i\Delta} \end{bmatrix} \begin{bmatrix} 1 & 0 \\ 0 & e^{i\delta} \end{bmatrix} \begin{pmatrix} 1 \\ 1 \end{pmatrix},$$

$$A_{\mathrm{Ref}} = \frac{1}{\sqrt{2}} \begin{bmatrix} 1 & 0 \\ 0 & e^{i\delta} \end{bmatrix} \begin{pmatrix} 0.6 \\ 0.6 \end{pmatrix}. \tag{9}$$

Finally, the test and reference beams pass through an analyzer with its transmission axis oriented at an angle ψ from horizontal. This gives the final Jones matrix representation of the test and reference beam amplitudes at the camera:

$$A_{\mathrm{Test}} = \frac{1}{\sqrt{2}} \begin{bmatrix} \cos(\psi)^2 & \cos(\psi)\sin(\psi) \\ \cos(\psi)\sin(\psi) & \sin(\psi)^2 \end{bmatrix} \begin{bmatrix} \cos(-\theta) & \sin(-\theta) \\ -\sin(-\theta) & \cos(-\theta) \end{bmatrix} \begin{bmatrix} 0.8\, e^{i\phi} & 0 \\ 0 & 1 \end{bmatrix} \begin{bmatrix} \cos(\theta) & \sin(\theta) \\ -\sin(\theta) & \cos(\theta) \end{bmatrix} \begin{bmatrix} e^{i\Delta} & 0 \\ 0 & e^{i\Delta} \end{bmatrix} \begin{bmatrix} 1 & 0 \\ 0 & e^{i\delta} \end{bmatrix} \begin{pmatrix} 1 \\ 1 \end{pmatrix},$$

$$A_{\mathrm{Ref}} = \frac{1}{\sqrt{2}} \begin{bmatrix} \cos(\psi)^2 & \cos(\psi)\sin(\psi) \\ \cos(\psi)\sin(\psi) & \sin(\psi)^2 \end{bmatrix} \begin{bmatrix} 1 & 0 \\ 0 & e^{i\delta} \end{bmatrix} \begin{pmatrix} 0.6 \\ 0.6 \end{pmatrix}. \tag{10}$$

The four amplitude components from the test and reference beams are added together to give the total amplitude at the camera. Multiplication of the amplitude by its complex conjugate gives the total intensity. The general form of the intensity as a function of all five variables, δ, Δ, ϕ, θ, and ψ, is too long and complex for presentation here but is presented in full elsewhere.[12] For each error analysis presented, all variables except the one under anal-

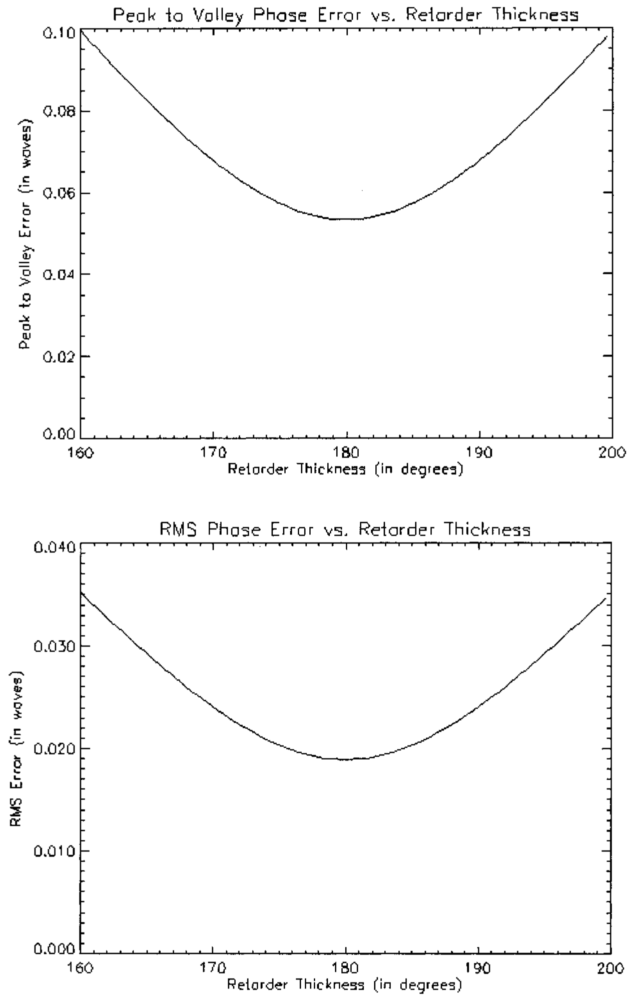

Fig. 7. Peak-to-valley and rms phase errors versus thin film retardance.

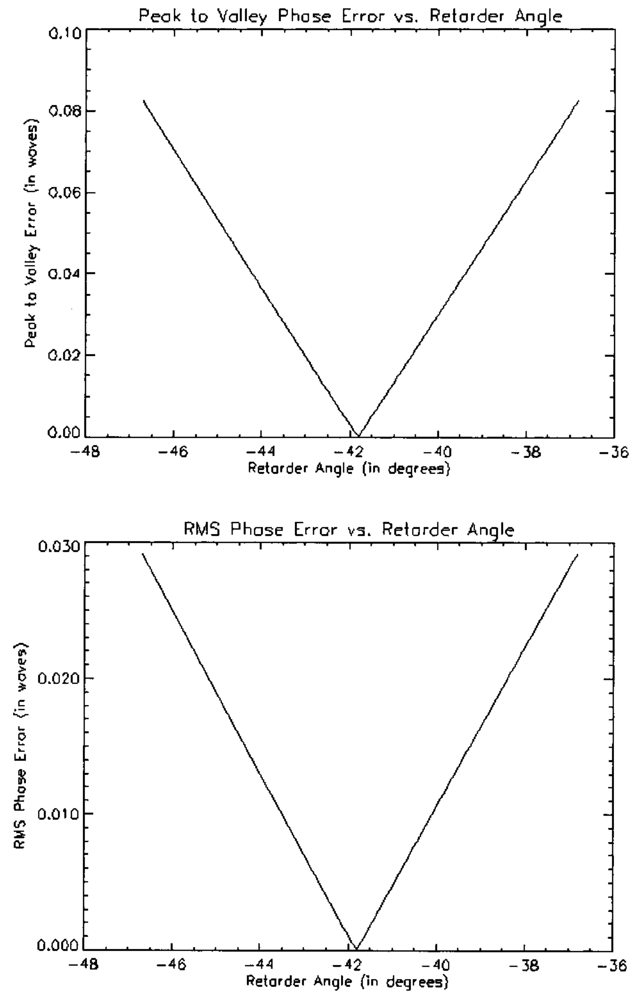

Fig. 8. Peak-to-valley and rms phase errors versus thin film alignment angle.

ysis are set to their ideal values, allowing an independent investigation of each error source to be made.

B. Retardance of the Thin Film

As stated above, the film used in the PPSPDI was measured on an Axometrics Muller matrix polarimeter and found to have a retardance of 160° ± 0.5° and a diattenuation of 20% ± 0.5%. We investigated the error resulting from the wrong retardance by setting the angle of the retarder, θ, to $-45°$ and the transmission axis of the final analyzer to horizontal. This gives a much simpler expression for the intensity at the camera as a function of δ, Δ, and ϕ only:

$$\begin{aligned} I(\delta,\ \Delta,\ \phi) = {} & 0.59 + 0.09\cos(\delta) + 0.03\cos(\Delta) \\ & + 0.03\cos(\delta+\Delta) + 0.2\cos(\delta-\phi) \\ & - 0.2\cos(\delta+\phi) + 0.24\cos(\Delta+\phi) \\ & - 0.24\cos(\delta+\Delta+\phi). \end{aligned} \tag{11}$$

Substituting values of 0°, 90°, 180°, and 270° for δ facilitates using the above intensity in a four-step phase-shifting algorithm and yields an equation for the output phase at the camera as a function of the retardance of the thin film and the surface phase from the test optic:

$$\text{Output phase} = \arctan \times \left[\frac{0.6\sin(\Delta) - 0.8\sin(\phi) - 0.48\sin(\Delta+\phi)}{0.18 + 0.6\cos(\Delta) - 0.48\cos(\Delta+\phi)}\right]. \tag{12}$$

In an ideal situation, the output phase would be identical to the input phase from the test optic, Δ; however, such is not the case. The error between the input phase from the test optic and the output phase at the camera is due to both the incorrect retardance of the thin film and the thin film's diattenuation. To calculate the phase error, set ϕ to a value and vary Δ from 0 to 2π, allowing for all possible phases from the test optic. The difference between the input phase and the output phase for each value of Δ is the phase error, and the peak-to-valley and rms phase errors are then determined for each value of ϕ. Because each input phase is used once, one may consider the peak-to-valley and rms errors to come from a uniform distribution of input phase and to be representative of actual data. This assumption is entirely reasonable because any interferogram with multiple fringes has a roughly uniform phase distribution from 0 to 2π. Figure 7 gives peak-to-valley and rms phase errors for ϕ ranging from 160° to 200°.

With $\phi = 180°$, the only source of error is the diattenuation of the film. With only the 20% diattenuation as a source of error, the peak-to-valley and the rms phase errors are 0.053 and 0.019 wave, respectively. Even with a perfect half-wave thin film, the diattenuation still limits the accuracy of the measured surface phase to approximately $\lambda/20$ peak to valley and $\lambda/50$ rms.

C. Angular Alignment of the Thin Film

Angular alignment of the thin-film retarder used to create the pinhole is the second major source of error for the PPSPDI. We determine errors that are due to the wrong angular alignment of the film by setting the film retardance to 180° and the transmission axis of the final analyzer to horizontal. This gives an intensity expression at the camera in terms of δ, Δ, and θ:

$$\begin{aligned} I(\delta, \Delta, \theta) = {} & 0.18 - 0.48 \cos(\Delta)\cos^2(\theta) + 0.32 \cos^4(\theta) \\ & - 1.08 \cos(\delta + \Delta)\cos(\theta)\sin(\theta) \\ & + 1.44 \cos(\delta)\cos^3(\theta)\sin(\theta) \\ & + 0.6 \cos(\Delta)\sin^2(\theta) + 0.82 \cos^2(\theta)\sin^2(\theta) \\ & - 1.8 \cos(\delta)\cos(\theta)\sin^3(\theta) + 0.5 \sin^4(\theta). \end{aligned} \tag{13}$$

Substituting values of 0°, 90°, 180°, and 270° for δ makes possible the use of intensity expression (13) in a four-step phase-shifting algorithm that results in an equation for the output phase at the camera as a function of the angle of the thin film, θ, and the surface phase from the test optic, Δ:

$$\text{Output phase} = \arctan\left[\frac{0.54 \cos(\Delta + 2\theta) - 0.54 \cos(\Delta - 2\theta)}{-0.36 \cos(\theta)\sin(\theta) - 2.16 \cos(\Delta)\cos(\theta)\sin(\theta) + 0.81 \sin(4\theta)}\right]. \tag{14}$$

The difference between the input phase from the test optic, Δ, and the output phase at the camera is a function of both the angular alignment of the film and the input phase. Setting the angular alignment of the film, θ, to zero gives an output phase of arc tan(0/0) that is undefined, showing that the interferometer does not phase shift because the polarization state of the beam passing through the film does not rotate as necessary for the instrument to operate. As in the previous case, θ is set to a value near the ideal value of 45° and Δ is varied from 0 to 2π, allowing for all possible phases from the test optic to determine the phase error. Subtracting the input phase from the output phase allows one to calculate the peak-to-valley and rms phase errors for each value of θ. Figure 8 gives the peak-to-valley and rms phase errors for θ ranging from −37° to −47°.

The minimum peak-to-valley and rms phase errors of 1.7×10^{-4} and 6.07×10^{-5} waves were found at −41.8° rotation of the thin film. With an ideal film retardance of 180°, the effect of the diattenuation is corrected by rotation of thin film to −41.8° instead of to −45°.

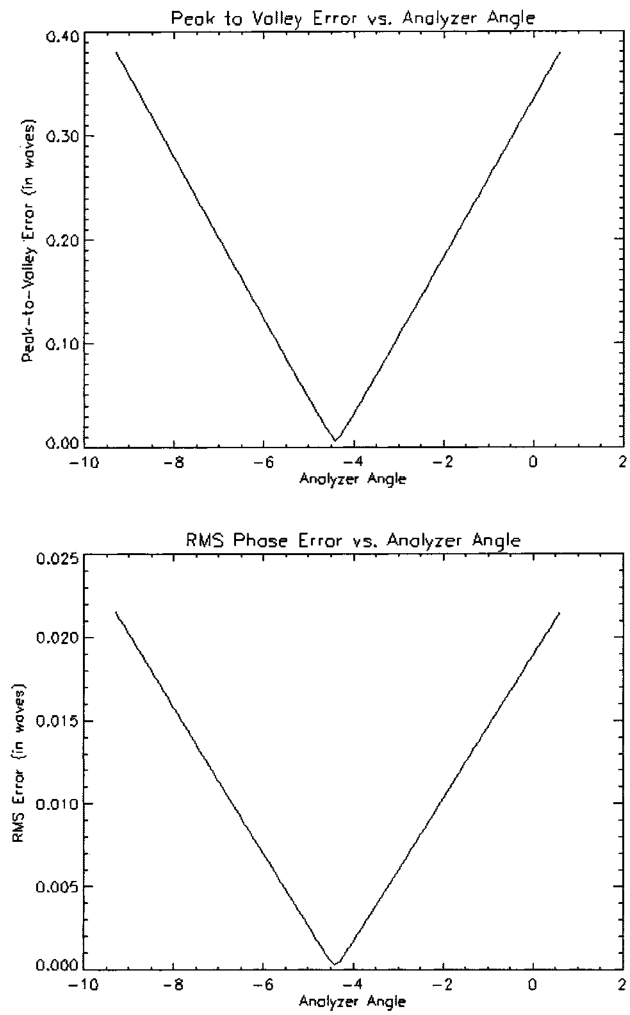

Fig. 9. Peak-to-valley and rms phase errors versus final analyzer angle.

D. Alignment of the Analyzer

The remaining source of error lies in the alignment of the transmission axis of the analyzer. To determine the error that is due solely to the analyzer, we set film retardance ϕ, to 180° and align it at $\theta = -45°$. The result is an intensity expression at the camera in terms of δ, Δ, and ψ. The intensity expression is too long and complex to be presented directly here but, again, is presented in full elsewhere.[12] Substituting values of 0°, 90°, 180°, and 270° for δ in the intensity expression permits using the intensity in a four-step phase-shifting algorithm, giving an equation for the output phase at the camera as a function of the alignment angle of the analyzer and the phase of the test optic:

$$\text{Output phase} = \arctan\left[\frac{0.27\cos(\Delta - 4\psi) - 0.27\cos(\Delta + 4\psi) + 1.08\cos(2\psi)\sin(\Delta)}{\begin{array}{l}0.77 + 1.14\cos(\Delta) - 0.03\cos(\Delta - 4\psi) - 0.59\cos(4\psi) - 0.03\cos(\Delta + 4\psi)\\ -0.6\sin(\Delta - 2\psi) + 0.6\sin(\Delta + 2\psi) + 2.72\cos(\psi)\sin(\psi)\end{array}}\right]. \tag{15}$$

The difference between input phase Δ and the calculated output phase at the camera is a function of both the input phase and the angle of the transmission axis of the final analyzer in the system. As in the other two cases referred to above, we set ψ to a value and vary Δ from 0 to 2π to determine the error for all possible phases from the test optic for each value of ψ. Subtracting the output phase from the input phase for all the Δ values allows the peak-to-valley and rms phase errors for each value of ψ to be determined. Figure 9 gives the peak-to-valley and rms phase errors for ψ ranging from 0° to $-9.5°$.

The minimum peak-to-valley and rms phase errors of 0.006 and 0.0003 wave are found at $-4.4°$. With a film retardance of 180°, rotating the transmission axis of the analyzer to $-4.4°$ from horizontal can significantly reduce the effect of the diattenuation.

The calculations show two possible ways to correct the phase error that is due to the diattenuation in the films: Rotate the film to $-41.8°$ instead of $-45°$ from vertical or rotate the transmission axis of the final analyzer to $-4.4°$ from horizontal. Both methods work well at correcting the phase error that is due to diattenuation, but rotating the retarder to $-41.8°$ provides the best result.

6. Quality of the Reference Wavefront

Just like any point-diffraction interferometer, the PPSPDI uses no reference optics; instead, it relies on diffraction from a pinhole to create a spherical reference wavefront. Ultimately, the quality of this reference wavefront will limit the accuracy of the PDI interferometer. Research has been conducted into the quality of the PDI's reference wavefront, but in each case the wavefront incident onto the pinhole was assumed to be a uniformly illuminated plane wave.[13] This is not a valid assumption because the amplitude and the phase incident onto the pinhole are neither uniform nor planar and depend on the aberrations of the test optic. Coma, spherical aberration, and astigmatism are investigated for pinhole sizes ranging from 50% to 150% of the unaberrated Airy disk diameter of the test optic.

A. Mathematical Model for Reference Wavefront Quality

This model begins at the test lens, represented by a cylinder function multiplied by an exponential phase term to include aberrations:

$$U(x_p, y_p) = \mathrm{cyl}\left[\frac{(x_p{}^2 + y_p{}^2)^{1/2}}{d_1}\right]\exp[i2\pi W(x_p, y_p)], \tag{16}$$

where $W(x_p, y_p)$ is the aberration function in units of waves with pupil coordinates x_p and y_p ranging from 0 at the center to 1 at the edge of the cylinder, describing all first- and third-order aberrations. The optical field from the test lens is brought to focus at the PDI plate, where the focus spot formed is the Fourier transform of the lens pupil function. For this model the pinhole is assumed to have perfect transmission, while the area outside the pinhole has zero transmission. This permits investigation of the reference wavefront independently of the test wavefront, because the test wavefront is not transmitted by the area around the pinhole. The field is multiplied by the pinhole, represented by a second cylinder function with diameter d_2, which has the effect of spatial filtering the field before the pinhole, removing the high frequencies and permitting transmission of only the lower frequencies:

$$U(x_2, y_2) = \mathcal{F}\left\{\mathrm{cyl}\left[\frac{(x_2{}^2 + y_2{}^2)^{1/2}}{d_1}\right]\exp[i2\pi W(x_2, y_2)]\right\} \times \mathrm{cyl}\left[\frac{(x_2{}^2 + y_2{}^2)^{1/2}}{d_2}\right], \tag{17}$$

where $\mathcal{F}$ represents a Fourier transform. After the pinhole, the optical field propagates to the far field, mathematically represented by a second Fourier transform of the field just after the pinhole. This produces the same effect as using a lens to image the field onto a camera, just as the actual operation of the interferometer does. Neglecting multiplicative constants yields the following optical field at the image plane:

$$U(x_3, y_3) = \mathrm{cyl}\left[\frac{(x_3{}^2 + y_3{}^2)^{1/2}}{d_1}\right]\exp[i2\pi W(x_3, y_3)] ** \mathcal{F}\left\{\mathrm{cyl}\left[\frac{(x_3{}^2 + y_3{}^2)^{1/2}}{d_2}\right]\right\}, \tag{18}$$

where (**) is a two-dimensional convolution across x and y.

There are two planes of interest in the model: the plane just before the pinhole and the final image plane. Determining the amplitude and the phase of the optical field before the pinhole will verify under what conditions, if any, the previously held assumption of a uniform plane wave striking the pinhole is valid. The variation in phase across the final image plane gives the error in the reference wavefront. The larger the variations in the phase, the worse the quality of the reference wavefront for the PPSPDI.

In the model, aberration values ranging from 0 to 6 waves of spherical aberration, coma, and astigmatism are applied to the test lens. In each case, the pinhole size is allowed to vary from 50% to 150% of the Airy disk diameter. Each aberration can then be analyzed separately as to its effect on the quality of the reference wavefront as a function of aberration magnitude and pinhole size.

B. Spherical Aberration

Spherical aberration is the first aberration used in the model, and, with spherical aberration only, the lens pupil function becomes

$$U(x_p,\ y_p) = \mathrm{cyl}\left[\frac{(x_p{}^2 + y_p{}^2)^{1/2}}{d_1}\right]\exp\left[i2\pi W_{40}(x_p{}^2 + y_p{}^2)^2\right], \tag{19}$$

where W_{40} is the number of waves of spherical aberration and the Fourier transform gives the optical field just before the pinhole.

For small values of spherical aberration, approximately two waves or fewer, and a pinhole diameter half the size of the diffraction-limited Airy disk, there is little variation in amplitude and phase across the pinhole, so the assumption of an incident plane wave is valid. But this assumption does not hold true for all values of spherical aberration, as the variations in phase and amplitude change as the amount of spherical aberration is varied. As the pinhole size increases to 100% or 150% of the Airy disk diameter, the variations in phase and amplitude increase and the incident plane-wave assumption is also no longer valid. Although there are special cases in which the plane-wave assumption is valid, in general, when the test wavefront incident onto the pinhole contains even small amounts of spherical aberration, the incident plane-wave assumption is invalid.

After multiplication by the pinhole, the optical field is Fourier transformed to simulate propagation to the final image plane. The peak-to-valley error of the phase of the optical field across the final image plane is calculated and gives the maximum error in the reference wavefront for the PPSPDI as a function of pinhole diameter and amount of spherical aberration. Figure 10 shows the reference wavefront error as a function of the amount of spherical aberration included in the model for pinhole diameters ranging from 50% to 150% of the unaberrated Airy disk diameter of the test optic.

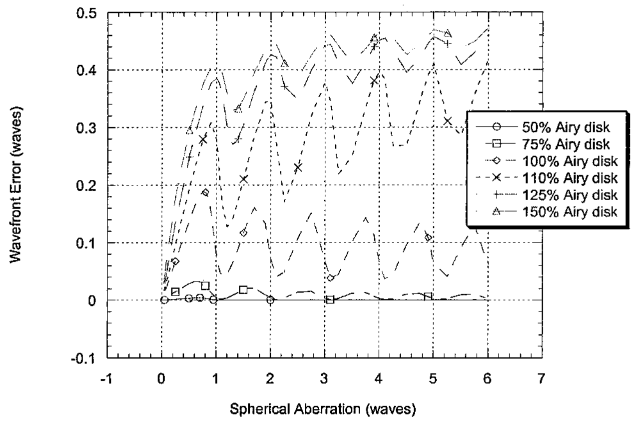

Fig. 10. Reference wavefront error versus spherical aberration for various pinhole sizes.

For a pinhole that is half of the Airy disk diameter, the maximum wavefront error of 0.004 wave occurs with 0.7 wave of spherical aberration added to the incident wavefront. This is the point of maximum variation in the amplitude and phase incident onto the pinhole. For pinhole diameters of 75% and 100% of the Airy disk, the maximum wavefront errors increase to 0.033 and 0.188 wave at 0.7 wave of added spherical aberration. This is the point of maximum variation in amplitude and phase for these larger pinhole sizes as well. It is apparent that for 0.7 wave of incident spherical aberration, the amplitude and the phase across the pinhole for all diameters less than the Airy disk are neither uniform nor planar and again invalidate the assumption of a uniformly illuminated plane wave striking the pinhole. For larger pinholes, the wavefront error increases dramatically to ~1 wave of added spherical aberration and then levels off, approaching 0.5 wave at 6 waves of added spherical aberration. There is a significant decrease in the amplitude of the oscillations of the wavefront error with increasing incident spherical aberration for all pinhole sizes.

Adding an equal but opposite amount of defocus to the spherical aberration to maximize the Strehl ratio reduces the reference wavefront error for pinholes up to the size of the test lens's Airy disk diameter. The addition of the defocus has the effect of minimizing the rms wavefront error at the pinhole. For a pinhole equal to the Airy disk diameter of the test lens, the maximum reference wavefront error is 0.188 wave at 0.7 wave of incident spherical aberration. Adding defocus reduces the maximum error in the reference wavefront to 0.046 wave at 2.5 waves of spherical aberration and −2.5 waves of defocus. This is a factor-of-four decrease in the reference wavefront error. For pinholes larger than the Airy disk diameter of the test lens, the effect of adding defocus to the incident wavefront is negligible.

As shown above, the larger the variations in amplitude and phase across the pinhole, the larger the error in the diffracted reference wavefront. Although this result is not unexpected, it does give insight into why it is a common practice to create a PDI pinhole whose diameter is no more than half of the unaberrated Airy disk diameter of the test optic. The smaller the pinhole diameter, the smaller the variations in amplitude and phase across the pinhole are, regardless of the incident aberrations. For a pinhole that is half of the Airy disk diameter of the test lens, the variations in amplitude and phase caused by spherical aberration cause a maximum error in the reference wavefront of only 0.004 wave.

C. Astigmatism

Astigmatism is the second aberration used in the model, and, looking only at astigmatism, the lens pupil function becomes

$$U(x_p,\ y_p) = \mathrm{cyl}\left[\frac{({x_p}^2 + {y_p}^2)^{1/2}}{d_1}\right]\exp\left[i2\pi W_{22}{y_p}^2\right], \tag{20}$$

where W_{22} is the number of waves of astigmatism added to the simulation. This function is Fourier transformed to give the optical field just before the pinhole. With a pinhole diameter equal to half of the unaberrated Airy disk diameter of the test lens and small amounts of astigmatism, neither the amplitude nor the phase of the wavefront at the pinhole can be considered uniform or planar. Once again, the immediate conclusion is the incident plane-wave assumption is invalid. In fact, this holds true for all values of astigmatism and pinhole size.

After multiplication by the pinhole, the optical field is Fourier transformed to simulate propagation to the final image plane. The peak-to-valley error of the phase of the optical field across the final image plane is calculated and gives the maximum error in the reference wavefront for the PPSPDI as a function of pinhole diameter and amount of astigmatism. Figure 11 shows the reference wavefront error as a function of the amount of astigmatism included in the model for pinhole diameters ranging from 50% to 150% of the unaberrated Airy disk diameter of the test optic.

In this case, there appear to be two distinct functional forms for the wavefront error, i.e., for pinholes less than the Airy disk diameter and for pinholes equal to or greater than the Airy disk diameter. Whereas again the wavefront error oscillates with increasing aberration for all pinhole sizes, for pinholes equal to the Airy disk diameter and greater, the wavefront error increases sharply to $\sim$1 wave of added astigmatism. Then the amplitude of the oscillation decreases, with the average value of the wavefront error approaching 0.5 wave at 6 waves of added astigmatism. For the smaller pinholes, the functional form is similar to the form found for spherical aberration, with an initial peak of $\sim$0.7 wave of added astigmatism and then a decrease in both the amplitude and the average value of the oscillation of the wavefront error with increasing astigmatism.

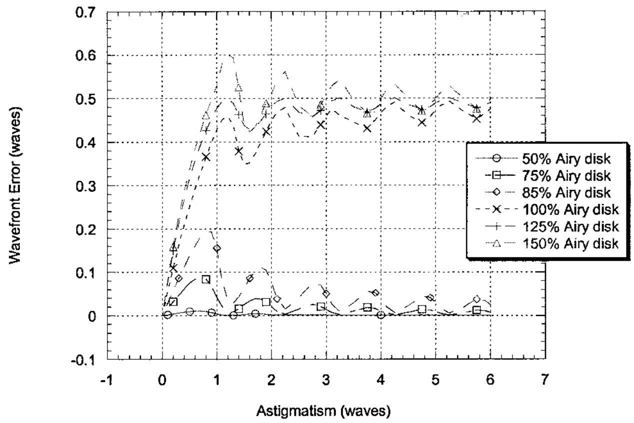

Fig. 11. Reference wavefront error versus astigmatism for various pinhole sizes.

D. Coma

Coma is the last aberration used in the simulation. With coma only, the lens pupil function becomes

$$U(x_p,\ y_p) = \mathrm{cyl}\left[\frac{({x_p}^2 + {y_p}^2)^{1/2}}{d_1}\right] \times \exp\left[i2\pi W_{31}({x_p}^2 + {y_p}^2)y_p\right], \tag{21}$$

where W_{31} is the number of waves of coma added for the simulation. This function is Fourier transformed to give the optical field just before the pinhole. Even with two waves of coma in the incident wavefront, the phase across a pinhole half the size of the Airy disk is planar. But the variations in amplitude keep the uniformly illuminated plane-wave approximation from being valid. As the pinhole size increases to 100% and 150% of the Airy disk diameter, the variations in amplitude increase along both profiles. Under no circumstances of pinhole size or incident amount of coma was the uniformly illuminated plane-wave approximation valid.

After multiplication by the pinhole, the optical field is Fourier transformed to simulate propagation to the final image plane. The peak-to-valley error of the phase of the optical field across the final image plane is calculated and gives the maximum error in the diffracted reference wavefront for the PPSPDI as a function of pinhole diameter and amount of coma added to the simulation. Figure 12 shows the reference wavefront error as a function of the amount of coma included in the simulation for pinhole diameters ranging from 25% to 150% of the unaberrated Airy disk diameter of the test optic. The pinhole diameter is reduced to 25% of the Airy disk diameter to successfully moderate the errors induced by the added coma.

For coma there appears to be only a single functional form for all pinhole sizes. There is an initial increase in the error to a peak that occurs from 0.7

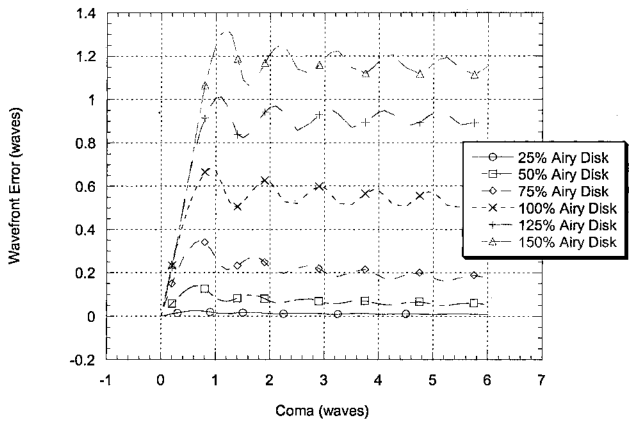

Fig. 12. Reference wavefront error versus coma for various pinhole sizes.

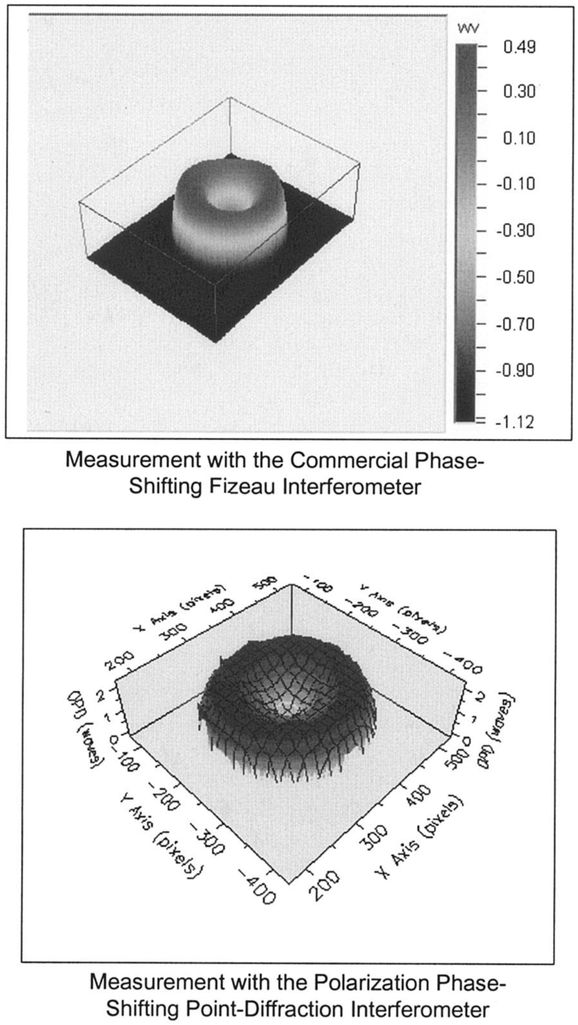

Fig. 13. Comparison of measurements of the test lens made with a commercial phase-shifting Fizeau interferometer and with the PPSPDI.

wave of coma for the 25% pinhole to 1.2 waves for the 150% pinhole, followed by the now expected oscillation of the wavefront error with increasing aberration. The amplitude of the oscillation decreases as the amount of added coma increases. Unlike in the previous two cases, the average value of the oscillations does not change with increasing aberration but remains relatively constant. For a pinhole that is one quarter of the Airy disk diameter, the maximum wavefront error in the diffracted wave is 0.026 wave at 0.7 wave of incident coma. For a pinhole that is one half of the Airy disk diameter, the maximum error increases to 0.14 wave at the same 0.7 waves of incident coma, the point of maximum variation in amplitude and phase at the pinhole for these pinhole sizes. This error is significantly larger than was found for both spherical aberration and astigmatism for the same pinhole size.

From these results, the diffracted reference wavefront is much more susceptible to errors that are due to coma in the incident beam than to either spherical aberration or astigmatism. For both spherical aberration and astigmatism, the variations in amplitude and phase across the pinhole are symmetric. Such is not the case with coma, as the shift in the central peak of the amplitude with increased aberration causes the amplitude variations across the pinhole to be nonsymmetric. This difference could account for the increased sensitivity of the reference wavefront to coma compared with spherical aberration and astigmatism.

7. Experimental Results

Before the performance of the PPSPDI can be presented, the specifics of the measurements must be discussed. The PPSPDI was set up as shown in Fig. 3 with the spatial filter positioned at twice the focal distance in front of the test lens to simulate a 4-*f* imaging system. The lens tested was a 42 mm diameter biconvex singlet with 200 mm focal length, giving an *f*-number of 4.75. In the 4-*f* configuration, the lens operated at an effective *f*-number of 9.5. Using a He–Ne laser at 0.6328 μm yielded a diameter of 14.7 μm for the diffraction-limited Airy disk formed at the rear focus of the lens. A pinhole diameter of 5 μm, 34% of the test lens Airy disk diameter, was used to minimize errors in the reference wavefront, improving the performance of the PPSPDI. Only approximately the center 70%, or 34 mm, of the lens could be tested because of the presence of large aberrations and high-frequency fringes near the edges of the interferograms that could not be resolved by the camera.

The best way to determine the accuracy of the PPSPDI is to compare a measurement with a calibrated instrument. Figure 13 shows the surface plots of the test lens obtained with the PPSPDI and with a commercial phase-shifting Fizeau interferometer.

The differences in Seidel coefficients for spherical aberration, astigmatism, and coma are 0.007, 0.144, and 0.171 wave, respectively. The coefficients for spherical aberration compare favorably. Although the coefficients for coma and astigmatism do not compare so well, the differences can be attributed to misalignment and tilt of the measured portion of the test lens from one instrument to the other. The difference in the astigmatism of 0.144 wave is caused by a difference in the tilt of the test lens between the two measurements. Assuming that there is no tilt of the test lens during the PPSPDI measurement, the difference of 0.144 wave is due to a tilt in the test lens when the measurement was made on the commercial Fizeau interferometer. Through simulations, the difference of 0.144 wave was found to be induced by a tilt angle of 0.61°. As the entire aperture of the lens was not tested, it is possible that the areas tested on the two instruments are slightly shifted. This would account for the difference in the coma values of 0.171 wave. We determine the amount of misalignment necessary to induce this coma by taking the difference of two shifted spherical aberration terms and setting it equal to the coma difference. With a measurement area radius of 17 mm, the shift in the two areas necessary to induce the 0.171 wave of coma is 70 μm.

The most important requirements when one is determining the performance of an interferometer are the accuracy and repeatability of the instrument. The accuracy of the instrument can be determined by comparison of a measurement with the same measurement on another instrument, done above. The repeatability gives an indication as to whether the interferometer results can be trusted from one measurement to the next and is determined by subtraction of two consecutive measurements. Figure 14 shows the subtraction of the two measurements.

The resultant rms error is 0.032 wave. This gives a system repeatability of just under $\lambda/30$. Careful inspection of Fig. 14 shows that the peaks in the error occur in what appear to be concentric rings occurring at roughly double the frequency of the fringes in the original interferograms. The most obvious cause of this error in the repeatability is phase-shift errors in the two measurements. The average phase shift across all frames in both measurements was found to be 90.85°, with a rms error of 2.1°. It is believed that the phase-shift error is due to the 20% diattenuation, which causes small fringe contrast changes from one phase-shifted interferogram to the next. The fringe contrast changes in successive interferograms were corrected in software before the final surface phase map was calculated, so the final phase error that resulted from the changes is negligible.

8. Discussion

In this paper we have described the development of a new interferometer, the polarization phase-shifting point-diffraction interferometer (PPSPDI). The PPSPDI uses a custom pinhole plate made by etching a pinhole into a bidirectionally deposited thin film, using a focused ion-beam etching technique, to separate the test and reference beams based on their polarization states. The half-wave birefringent pinhole plate, along with a polarizer, interfere what begin as orthogonally polarized test and reference beams, which can be phase shifted by

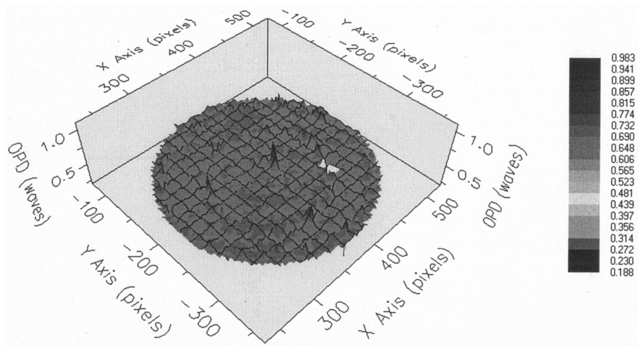

Fig. 14. Subtraction of two consecutive measurements: OPDs, optical path differences.

application of a voltage to an electro-optic modulator located next to the laser source.

The most significant limitation in the PPSPDI is the birefringent thin film used to create the half-wave-plate pinhole filter. The wrong retardance along with significant diattenuation caused problems in getting the PPSPDI to operate correctly. Considering the problems with the thin films, the PPSPDI's performance was admirable. The measurement of the test lens on the PPSPDI compared favorably with the result for the same lens on the commercial interferometer. Subtracting two consecutive measurements demonstrated a measurement repeatability of better than $\lambda/30$. Correcting the problems in the deposition of the thin films would significantly improve the performance of the PPSPDI.

The authors thank Ian Hodgkinson and Qihong Wu of The University of Otago, New Zealand, for providing numerous sets of thin films and Engineering Synthesis Design, Inc., for donating a copy of Intelliwave (phase-shift control software) to control the PPSPDI.

References

1. O. Y. Kwon, "Multichannel phase-shifted Interferometer," Opt. Lett. **9,** 59–61 (1984).
2. H. Kadono, T. Nobukatsu, and T. Asakura, "New common-path phase shifting interferometer using a polarization technique," Appl. Opt. **26,** 898–904 (1987).
3. H. Kadono, M. Ogusu, and S. Toyooka, "Phase shifting common path interferometer using a liquid-crystal phase modulator," Opt. Commun. **110,** 391–400 (1994).
4. C. R. Mercer and K. Creath, "Liquid-crystal point-diffraction interferometer for wave-front measurements," Appl. Opt. **35,** 1633–1642 (1996).
5. M. Totzeck, N. Kerwein, A. Tavrov, E. Rosenthal, and H. J. Tiziani, "Quantitative Zernike phase-contrast microscopy by use of structured birefringent pupil-filters and phase-shift evaluation," in *Interferometry XI: Techniques and Analysis,* K. Creath and J. Schmit, eds., Proc. SPIE **4777,** 1–11 (2002).
6. J. C. Wyant, "Recent Investigations of interferometry and applications to optical testing," in *Los Alamos Conference on Optics 1979*, D. H. Liebenberg, ed., Proc. SPIE **190,** 507–511 (1979).
7. W. H. Steel, *Interferometery* (Cambridge U. Press, 1983).
8. I. J. Hodgkinson and Q. H. Wu, *Birefringent Thin Films and Polarizing Elements* (World Scientific, 1997).
9. I. Hodgkinson and Q. H. Wu, "Review of birefringent and chiral optical interference coatings," in *Optical Interference Coating,*

2001 OSA Technical Digest (Optical Society of America, 2001), pp. FA1–FA3.
10. A. Street, “How a FIB works,” Integrated Reliability, retrieved 22 May, 2002, http://www.irsi.com/Site1/fibwork.html.
11. C. Friedrich, “Micromilling tools,” Michigan Technological University, Department of Mechanical Engineering–Engineering Mechanics, retrieved 22 May 2002, http://www.me.mtu.edu/~microweb/chap7/ch7-1.htm (1998).
12. R. M. Neal, “Polarization phase-shifting point-diffraction interferometer,” Ph.D. dissertation (University of Arizona, 2003).
13. K. A. Goldberg, E. Tejnil, and J. Bokor, “A 3-D numerical study of pinhole diffraction to predict the accuracy of EUV point diffraction interferometry,” in *Extreme Ultraviolet Lithography*, Vol. 4 of OSA Trends in Optics and Photonics (Optical Society of America, 1996), pp. 133–137.